Computers and Geotechnics 172 (2024) 106413

Contents lists available at ScienceDirect

Computers and Geotechnics

journal homepage: www.elsevier.com/locate/compgeo

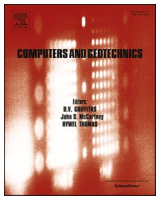

Research Paper

Probabilistic assessment of 3D slope failures in spatially variable soils by cooperative stochastic material point method

Shui-Hua Jiang [a], Jian-Ping Li [a], Guo-Tao Ma [b,c,*], Mohammad Rezania [b]

[a] School of Infrastructure Engineering, Nanchang University, 999 Xuefu Road, Nanchang 330031, China
[b] School of Engineering, The University of Warwick, Coventry CV4 7AL, United Kingdom
[c] Faculty of Geosciences and Environmental Engineering, Southwest Jiaotong University, 611756 Chengdu, China

ARTICLE INFO

Keywords:
Spatial variability
Slope large deformation
Failure mode
Cooperative stochastic material point method
Probabilistic analysis

ABSTRACT

Accurate assessment of slope failures and their large deformations is critical for effective landslide mitigation. This study introduces the new Cooperative Stochastic Material Point Method (CSMPM), addressing challenges in probabilistic characterization of slope large deformations considering three-dimensional (3D) soil heterogeneities. The method employs an enhanced Karhunen-Loève (KL) expansion to model 3D soil spatial variability efficiently. By using rough and refined grids, derived through the enhanced KL expansion, the study achieves computational efficiency without compromising accuracy. By combining the computational advantages of the rough grid with the precision of the refined grid, the CSMPM enables efficient probabilistic analysis of 3D heterogeneous slopes. The results demonstrate its capability to identify slope large deformation failure modes and quantify the associated failure probability. Notably, the shallow failure mode exhibits fan-shaped horizontal diffusion, introducing uncertainty, while the compound failure mode presents challenges in landslide prevention. The progressive failure mode poses the highest hazard. Horizontal heterogeneities significantly influence both large deformation likelihood and failure modes, emphasizing the importance of 3D soil spatial variability in geotechnical reliability assessments. The CSMPM, with its innovative approach, proves to be a practical tool for enhancing our understanding of geohazards and associated uncertainties, as well as large deformations. It provides valuable insights for improving risk assessment of slope hazards.

1. Introduction

Landslides are one of the most common natural geological hazards in the world (e.g., Bandara et al., 2016; Zhang et al., 2018; Jiang et al., 2022a; Troncone et al., 2023). In particular, the phenomenon of large deformations in the landslides, which dynamically progresses due to slope instability, presents a significant threat to adjacent infrastructure and human safety (e.g., Mohammadi and Taiebat, 2013; Chen et al., 2021). Different geomaterials, originating from intricate geological processes, inherently display spatial variability or heterogeneity in their physical and mechanical attributes, reflecting the multifaceted nature of their formative processes (e.g., Jiang et al., 2014; Deng et al., 2017; Chen et al., 2022; Liu et al., 2022). There is evidence that spatial variability of soil shear strength parameters significantly influences slope failures, where slopes are susceptible to instability, and failures typically occur along paths of minimal resistance (e.g., Ma et al., 2022a; Chen et al., 2021). The soil heterogeneity significantly affects the slope failure modes and mechanisms, as well as the probability of failure and post-failure behavior of the slope (e.g., Liu et al., 2019; Chen et al., 2022). Although extensive research has been conducted on the effects of spatial variability in soil properties on two-dimensional slope failures, very limited research has been conducted on 3D slope failures that consider the spatial variability of soil parameters (Jiang et al., 2022a). Recent works, by Li et al. (2015) and Shu et al. (2023), have demonstrated that the 3D spatial variability of geotechnical parameters has a significant impact on slope failure mechanisms. Therefore, international standards (Phoon et al., 2016) emphasize the importance of modelling that accounts for this 3D spatial variability in the geotechnical parameters in order to facilitate slope failure analysis and associated risk assessments.

Currently, there are several simulation methods that are available to model the 3D spatial variability of geotechnical parameters (as shown in Table 1), such as, discrete cosine transform method (Wang et al., 2021),

* Corresponding author at: School of Engineering, The University of Warwick, Coventry CV4 7AL, United Kingdom.
E-mail addresses: sjiangaa@ncu.edu.cn (S.-H. Jiang), jianping_lee@email.ncu.edu.cn (J.-P. Li), derek.ma.1@warwick.ac.uk (G.-T. Ma), m.rezania@warwick.ac.uk (M. Rezania).

https://doi.org/10.1016/j.compgeo.2024.106413
Received 23 December 2023; Received in revised form 31 March 2024; Accepted 7 May 2024
Available online 24 May 2024

Fourier transform technique (Hu et al., 2022), and stepwise covariance matrix decomposition method (e.g., Li et al., 2019; Zhang et al., 2022), etc. Among them, the Karhunen-Loève (KL) expansion method is widely employed to simulate the spatial variability of soil parameters due to its ability to obtain accurate results with fewer truncation terms (Phoon et al., 2002). However, in the context of simulating the 3D spatial variability of geotechnical parameters over extensive scales, and especially within the limited scales of fluctuation, the computational demand can be prohibitively high. As such, the KL expansion method is rarely used in the simulation of the 3D spatial variability of geotechnical parameters.

In Huang et al. (2013) the landslide risk was defined as the product of landslide probability and landslide consequences. Due to the difficulty in modeling the large deformations of the slope, most studies have only focused on quantifying the probability of 3D slope failure using either the random limit equilibrium method (RLEM) or the random finite element method (RFEM). For example, Hicks et al. (2014) studied the influence of the 3D heterogeneity of undrained shear strength on the reliability and risk of clay slopes at different depths using the RFEM. Xiao et al. (2016) proposed using an auxiliary RFEM method for 3D slope risk assessment. Liu et al. (2018) used the RFEM method to calculate the probability of slope failure based on the critical cross-section of a 3D slope. Hu et al. (2022) investigated the influence of the 3D spatial variability of soil parameters on the slope failure mechanism using the RLEM. The existing research primarily focuses on the pre-failure and initiation phases of slopes, overlooking the critical post-onset period marked by extensive large deformation failures. Following the initiation of slope instability, the finite element mesh undergoes distortion, rendering the conventional methods such as the RLEM and RFEM, that have been developed for small deformations, unsuitable for simulating the comprehensive process of large deformation failures (e.g., Jiang et al., 2022a; Ma et al., 2022a,2022b,2022c). The large deformation characteristics, which serve as indicators of the consequences of slope failures, are integral to effective landslide risk assessment. However, the quantitative risk assessment based on the large deformation characteristics of 3D slopes presents a considerable challenge (e.g., Chen et al., 2021; Jiang et al., 2022a; Liu et al., 2022). In light of this, there is a need for advanced methodologies that can capture and analyze the intricate details of large deformation failures in the 3D slopes.

Advanced numerical techniques, including discrete element method (DEM) (Weng et al., 2019), discontinuous deformation analysis (DDA) (Chen and Wu, 2018), coupled Eulerian-Lagrangian (CEL) (e.g., Chen et al., 2021; Liu et al., 2022), smoothed particle hydrodynamics (SPH) method (Zhang et al., 2020) and material point method (MPM) (e.g., Soga et al., 2016; Coombs et al., 2020; Yerro et al., 2022; Jiang et al., 2022b), have been used to overcome the mesh distortions when modeling the slope large deformations. In recent years, the MPM has become a powerful tool for simulating the entire process of slope large deformation failure due to its integration of the advantages of Lagrangian and Eulerian methods, including high computational accuracy (Zhang et al., 2016). Bandara et al. (2016) used the MPM to simulate the entire process of a rainfall-induced landslide. Conte et al. (2020) applied the MPM to model the runout process of the Maierato

Table 1
Research on probabilistic stability analysis of three-dimensional slopes considering spatial variability of soil parameters.

No.	Analysis method	Random field parameter information					Geometric parameter			Source
		Soil parameters	Probability distribution	Autocorrelation function	Autocorrelation distance (m)	Random field discretization Method	Slope angle (°)	Slope height (m)	Longitudinal length (m)	
1	FEM	S_u	Normal	Exponential Gauss–Markov	$l_h = 1$–1000, $l_v = 1$	LAS	45	5	100	Hicks et al. (2014)
2	FEM	S_u	Normal	Exponential Gauss–Markov	$l_h = 1$–12, $l_v = 1$	LAS	45	5	50	Li et al. (2015)
3	FEM	S_u	Lognormal	Squared exponential	$l_h = 20$, $l_v = 2$	EOLE	26.6	6	100	Xiao et al. (2016)
4	FEM	S_u	Lognormal	Squared exponential	$l_h = 10$, $l_v = 2$	MLEM	26.6	5	30, 60	Liu et al. (2018)
5	LEM	S_u	Normal	Single exponential	$l_h = 10$, $l_v = 1$	FFT	30	10	500	Lee and Ching (2020)
6	CEL	c, φ	Lognormal	Squared exponential	$l_h = 20$, $l_v = 4$	MLEM	26.6	10	0–150	Chen et al. (2021)
7	FEM	S_u	Lognormal	Squared exponential	$l_h = 1$–60, $l_v = 1$	CMD	45	5	60	Huang and Leung (2021)
8	FEM	c, φ	Normal	/	$l_h = 25$, $l_v = 2$	DCT	26.6	15	50	Wang et al. (2021)
9	LEM	c, φ, γ	Normal	Squared exponential	$l_h = l_v = 2$–40	FFT	30, 45, 60	40	100	Hu et al. (2022)
10	CEL	c, φ	Lognormal	Squared exponential	$l_h = 20$, $l_v = 4$	MLEM	26.6	10	100	Liu et al. (2022)
11	FEM	S_u, k_s	Lognormal	Single exponential	$l_h = 24$, $l_v = 1$	CMD	45	5	20	Ng et al. (2022)
12	FDM	c, φ	Lognormal	Single exponential	$l_h = l_v = 4$	CMD	45	10	15	Zhang et al. (2022)
13	FEM	c, φ	Lognormal	Gaussian	$l_h = 1$–1000, $l_v = 1$	LAS	45	9	50	Varkey et al. (2023)
14	LEM	S_u	Lognormal	Exponential Gauss–Markov	$l_h = l_v = 10$	SRM	18.4, 26.6, 45	10	100	Shu et al. (2023)

Note: FEM, FDM, LEM and CEL denote the finite element method, finite difference method, limit analysis method and coupled Euler-Lagrange method, respectively; c, φ, γ, S_u and k_s represent the cohesion, internal friction angle, unit weight, undrained shear strength and saturated permeability coefficient, respectively; l_h and l_v denote the horizontal and vertical autocorrelation distances, respectively; CMD, LAS, MLEM, DCT, FFT, SRM and EOLE represent the covariance matrix decomposition method, local average subdivision method, modified linear estimation method, discrete cosine transform method, Fourier transform technique, spectral representation method and extended optimal linear estimation method, respectively.

landslide. Another advantage of the MPM is that it can utilize history-dependent constitutive models. Since the landslides may result in extensive shearing of soils, it is important to select an appropriate constitutive model that can capture the critical state as well as the residual state (Soga et al., 2016). Yerro et al. (2016) used the MPM to simulate the entire process of slope instability incorporating the Mohr-Coulomb model with strain softening behavior induced by increasing deviatoric plastic strain. Troncone et al., (2022a) utilized the MPM combined with a strain-softened Mohr-Coulomb constitutive model to simulate the deformation process occurring in landslides. Troncone et al., (2022b) further proposed an analytical method to reduce the influence of the grid dependence on the numerical results.

To incorporate the inherent spatial variability of soil properties, Wang et al. (2016) first combined the theory of random fields (RFs) with the MPM, proposing the random material point method (RMPM). Liu et al. (2019) developed the efficient computation of the random limit equilibrium and MPM to calculate the probability of slope large deformation failure. Ma et al., (2022a,2022b) applied the stochastic material point method (SMPM) to simulate a series of granular flows and post-failure motions in landslides, accounting for diverse soil heterogeneities. However, in engineering practice, slopes manifest in 3D, and understanding the genuine internal failure mechanisms necessitates 3D modeling. Moreover, Chowdhury and Xu (1995) highlighted the correlation among multiple failure modes of the slope. Presently, a gap exists in the research regarding the evolution of various large deformation failure modes in the context of 3D heterogeneous slopes and the impact of the 3D spatial variability of soil parameters on these failure modes. This gap likely stems from the computational challenges associated with the SMPM, leading to an unexplored research area. Thus, there is a need for an efficient SMPM that can automatically identify the failure modes while alleviating the computational complexities inherent in the 3D heterogeneous slope large deformation analysis. Bridging this gap will significantly contribute to advancing our understanding of the landslide processes, particularly in realistic 3D slope scenarios, and enhance the accuracy of predictive models for more effective risk assessment of slope failures.

Addressing the computational challenges inherent in calculating the probability of 3D slope large deformation failure using the SMPM necessitates a novel approach. This paper introduces a new Cooperative Stochastic Material Point Method (CSMPM) for 3D slopes, accompanied by an enhanced KL expansion technique to simulate the 3D spatial variability of soil parameters. The core concept involves developing two distinct sets of background grid models in the MPM to enable collaborative analysis. The proposed approach encompasses two essential modules: (1) Discretization of 3D RFs concerning the soil parameters; (2) Collaborative analysis of significant slope large deformations using the rough and refined grid models. Importantly, this methodology is agnostic to the coordinates of RF grids, seamlessly integrating the two distinct grid models for both roughening and refinement processes.

The paper is structured as follows: The "Methodology" section details the new CSMPM, wherein the 3D RF implementations are generated through an enhanced KL expansion technique coupled with a Latin hypercube sampling method. Subsequently, the "Illustrative Example" section presents a 3D clay slope as a representative case to demonstrate the effectiveness of the proposed approach. The analysis explores in detail the evolution mechanism, failure process and hazards of the four identified failure modes in detail. Furthermore, an exploration of the influence of horizontal autocorrelation distance on both the slope large deformation failure modes and the associated failure probability is conducted. The "Discussion" section investigates the further improvement room of the proposed approach. This comprehensive framework contributes to advancing our understanding of 3D slope post-failure behaviors, offering a valuable tool for enhanced risk assessments in geotechnical engineering.

2. Methodology

2.1. Generation of 3D random fields using enhanced Karhunen-Loève expansion method

The KL expansion method is a spectral method based on the decomposition of the autocorrelation function (Jiang et al., 2022a). However, its application in the context of 3D slopes is relatively limited. This is mainly because, once extended to three dimensions, a huge autocorrelation coefficient matrix needs to be decomposed. In addition, although this method can achieve similar accuracies to other methods with a smaller number of truncation terms, its computational efficiency is relatively low, especially for the 3D problems. Additionally, this method encounters the dual challenges of memory space and computational load. Fortunately, Li et al. (2019) and Zhu et al. (2021) proposed a decomposed KL expansion method that is suitable for characterizing the spatial variability of soil parameters in the three dimensions with large sizes and small scales of fluctuation. Firstly, the widely used separable 3D isotropic squared exponential autocorrelation function is employed to characterize the spatial autocorrelation of soil parameters:

$$\rho(\tau_x)\rho(\tau_y)\rho(\tau_z) = \exp\left(-\frac{\tau_x^2}{l_x^2}\right)\exp\left(-\frac{\tau_y^2}{l_y^2}\right)\exp\left(-\frac{\tau_z^2}{l_z^2}\right) \tag{1}$$

where τ_x, τ_y and τ_z are the distances between any two points in space along the X, Y, and Z directions, $\tau_x = x_i - x_j$, $\tau_y = y_i - y_j$, $\tau_z = z_i - z_j$, respectively; l_x, l_y, and l_z represent the autocorrelation distances in the X, Y, and Z directions, respectively. Next, the KL expansion method is adopted to discretize the Gaussian RFs of soil parameters, and the matrix operation process for generating the Gaussian RFs of soil parameters can be expressed as (Jiang et al., 2014)

$$\boldsymbol{H} = \mu + \left[\sigma \mathrm{diag}\left(\sqrt{\lambda}\right)\boldsymbol{F}^{\mathrm{T}}\right]^{\mathrm{T}}\boldsymbol{W} \tag{2}$$

where μ and σ represent the mean and standard deviation of a soil parameter, respectively; $\boldsymbol{H}$ is the matrix for implementing the soil parameter with a dimension of $m \times 1$, where m is the number of RF grids; $\mathrm{diag}\left(\sqrt{\lambda}\right)$ is an $N \times N$ diagonal matrix composed of N eigenvalues; $\boldsymbol{W}$ is a standard normal random vector with a dimension of $N \times 1$, $\boldsymbol{W} = (\xi_1, \xi_2, \cdots, \xi_N)^{\mathrm{T}}$; $\boldsymbol{F}$ is the matrix of eigenfunctions with a dimension of $m \times N$, expressed as

$$\boldsymbol{F} = \begin{bmatrix} \varphi_1(x_1, y_1, z_1) & \varphi_2(x_1, y_1, z_1) & \cdots & \varphi_N(x_1, y_1, z_1) \\ \varphi_1(x_2, y_2, z_2) & \varphi_2(x_2, y_2, z_2) & \cdots & \varphi_N(x_2, y_2, z_2) \\ \vdots & \vdots & \vdots & \vdots \\ \varphi_1(x_m, y_m, z_m) & \varphi_2(x_m, y_m, z_m) & \cdots & \varphi_N(x_m, y_m, z_m) \end{bmatrix} \tag{3}$$

where $\varphi_j(x_i, y_i, z_i)$ are the eigenfunction values at different locations corresponding to the j-th eigenvalue, $i = 1, 2, \ldots, m$, $j = 1, 2, \ldots, N$. For the 3D autocorrelation coefficient matrix, directly performing eigenvalue decomposition requires a large amount of memory space, which may even exceed the memory capacity of a regular computer. In contrast, converting the direct decomposition of a 3D autocorrelation coefficient matrix into the decomposition of three one-dimensional autocorrelation coefficient matrices can significantly improve the computational efficiency. The 3D autocorrelation coefficient matrix can be represented as

$$\boldsymbol{R} = \boldsymbol{R}_x \otimes \boldsymbol{R}_y \otimes \boldsymbol{R}_z \tag{4}$$

where $\boldsymbol{R}_x$, $\boldsymbol{R}_z$, and $\boldsymbol{R}_z$ are the one-dimensional autocorrelation coefficient matrices after decomposition; $\otimes$ expresses as a Kronecker product. The corresponding matrices of eigenvalues and eigenfunctions can be expressed as

$$\boldsymbol{\lambda} = \boldsymbol{\lambda}_x \otimes \boldsymbol{\lambda}_y \otimes \boldsymbol{\lambda}_z \tag{5}$$

$$\boldsymbol{F} = \boldsymbol{F}_x \otimes \boldsymbol{F}_y \otimes \boldsymbol{F}_z \tag{6}$$

To obtain the eigenvalues and eigenfunctions of an autocorrelation function, it is necessary to solve the Fredholm integral equation of the second kind (e.g., Phoon et al., 2002; Jiang et al., 2014, 2023). Taking the X direction as an example, the expression is calculated as follows:

$$\int_{\Omega} \rho_x(x_1, x_2)\varphi_k(x_2)dx_2 = \lambda_k \varphi_k(x_1) \tag{7}$$

where x_1 and x_2 are the coordinates of any two points in the one-dimensional computational region Ω. However, the Fredholm integral equation of the second kind has an analytical solution only for triangular or single exponential autocorrelation functions (Zhu and Hiraishi, 2023). Numerical methods are necessary to solve for the eigenvalues and eigenfunctions of the equation in all other cases. This study employs the wavelet-Galerkin technique (Phoon et al., 2002) to solve the integral equation in Eq. (7) numerically. Initially, the eigenfunction in the Haar wavelet basis can be represented as

$$\varphi_k(x) = \sum_{i=0}^{N-1} d_i^{(k)} \psi_i(x) = \boldsymbol{\Psi}^T(x)\boldsymbol{D} \tag{8}$$

The autocorrelation function is also expressed in Haar wavelet basis as

$$\rho_x(x_1, x_2) = \sum_{i=0}^{N_k-1} \sum_{j=0}^{N_k-1} \overline{A_{ij}} \psi_i(x_1)\psi_j(x_2) = \boldsymbol{\Psi}^T(x_1)\overline{\boldsymbol{A}}\boldsymbol{\Psi}(x_2) \tag{9}$$

$$\overline{A_{ij}} = \frac{1}{h_i h_j} \int_0^1 \int_0^1 \rho_x(x_1, x_2)\psi_i(x_2)\psi_j(x_1)dx_1 dx_2 \tag{10}$$

where $N_k = 2^t$, t is the maximum wavelet level; $d_i^{(k)}$ is the wavelet coefficient; $\Psi_i(.)$ is the Harr wavelet basis function; $\overline{\boldsymbol{A}}$ is the 2D wavelet transformation matrix of the autocorrelation function with a dimension of $N_k \times N_k$; h_i is a constant that can be determined by the orthogonality condition of the Harr wavelet basis. By substituting Eqs. (8)-(10) into Eq. (7), respectively, the eigenvalue problem for the Fredholm integral equation can be transformed into a finite eigenvalue problem as follows:

$$\lambda \boldsymbol{\Psi}^T(x)\boldsymbol{D} = \boldsymbol{\Psi}^T(x)\overline{\boldsymbol{A}}\boldsymbol{P}\boldsymbol{D} \tag{11}$$

where $\boldsymbol{P}$ is the diagonal matrix, which can be expressed as

$$\boldsymbol{P} = \begin{bmatrix} h_0 & \cdots & 0 \\ \vdots & \ddots & \vdots \\ 0 & \cdots & h_{N_k-1} \end{bmatrix} \tag{12}$$

Given that $\widehat{\boldsymbol{D}} = \boldsymbol{P}^{1/2}\boldsymbol{D}$, $\widehat{\boldsymbol{A}} = \boldsymbol{P}^{1/2}\overline{\boldsymbol{A}}\boldsymbol{P}^{1/2}$, thus Eq. (11) can be further converted as

$$\lambda \widehat{\boldsymbol{D}} = \widehat{\boldsymbol{A}}\widehat{\boldsymbol{D}} \tag{13}$$

Then the eigenvalue decomposition of Eq. (13) is carried out to obtain the eigenvector $\widehat{\boldsymbol{D}}$ and the eigenvalue λ of the autocorrelation function, and further the wavelet inverse transform of the eigenvector $\widehat{\boldsymbol{D}}$ is carried out to obtain the eigenfunction of the autocorrelation function as follows:

$$\boldsymbol{F} = \boldsymbol{\Psi}^T(x)\boldsymbol{P}^{-1/2}\widehat{\boldsymbol{D}} \tag{14}$$

In this way, the eigenvalues and eigenfunctions of the autocorrelation function for each dimension can be obtained. Then, substituting Eqs. (5) and (6) into Eq. (2), we get the Gaussian RF implementation as follows:

$$\boldsymbol{H} = \mu + \left\{ \sigma \left[\mathrm{diag}\left(\sqrt{\lambda_x}\right)\boldsymbol{F}_x^{\mathrm{T}} \right] \otimes \left[\mathrm{diag}\left(\sqrt{\lambda_y}\right)\boldsymbol{F}_y^{\mathrm{T}} \right] \otimes \left[\mathrm{diag}\left(\sqrt{\lambda_z}\right)\boldsymbol{F}_z^{\mathrm{T}} \right] \right\}^{\mathrm{T}} \boldsymbol{W} \tag{15}$$

Finally, based on the statistical characteristics of the soil parameter [i.e., mean, coefficient of variation (COV), and marginal distribution], the Gaussian RF implementation is transformed through equiprobable transformation to obtain the non-Gaussian RF implementation as follows (Jiang et al., 2014):

$$\boldsymbol{H}^{NG} = G^{-1}[\Phi(\boldsymbol{H})] \tag{16}$$

where $\boldsymbol{H}^{NG}$ is the non-Gaussian RF matrix; $G^{-1}(\cdot)$ is the inverse cumulative distribution function of the marginal distribution of $\boldsymbol{H}$; $\Phi(\cdot)$ is the cumulative distribution function of a standard normal variable. The transformation method through matrix operations greatly simplifies the process of eigenvalue decomposition of the autocorrelation coefficient matrix, overcoming the limitation of exceeding computer memory when decomposing the huge 3D autocorrelation coefficient matrix. This method significantly improves the generation speed of 3D RFs for soil parameters (e.g., Li et al., 2019; Zhu et al., 2021).

2.2. Validation of the enhanced KL expansion technique via two examples

While the enhanced KL expansion technique significantly accelerates the RF generation process, its influence on both the precision of RF generation and the subsequent results of probabilistic calculations remains unknown. To address this challenge, two illustrative examples are employed to rigorously assess the accuracy of the enhanced KL expansion technique in generating the 3D RFs.

Example 1. *The proposed approach in this study is applied to an undrained cohesive slope previously studied by* Cho (2010). *The slope is extended by an additional* 10 m *in the Y direction, creating a* 3*D model of the slope to verify the effectiveness of the enhanced KL expansion technique. In total,* 18,200 *finite difference grids are divided into different types*: 18,000 *hexahedra and* 200 *wedges. These grids are composed of* 20,601 *nodes.*

The mean of the undrained shear strength (S_u) is 10 kPa, the COV is 0.3, and it follows the lognormal distribution. The squared exponential autocorrelation function in Eq. (1) is used to simulate the spatial autocorrelation of S_u. The RF grids are consistent with the finite difference grids. The grid size is 0.5 m × 0.5 m × 0.5 m, the horizontal autocorrelation distance is 16.9 m (in the X and Y directions), and the vertical autocorrelation distance is 1.7 m (in the Z direction). When the number of eigenmodes $n = 30$, the ratio of the expected energy $\varepsilon \geq 95\,\%$ can be satisfied (Jiang et al., 2014). Fig. 1 compares the simulated values and theoretical values of the autocorrelation coefficients of S_u in the three directions at a reference point, which is located at the center of the slope (9.75 m, 4.75 m, 4.75 m). The theoretical values of the autocorrelation coefficients of S_u in Fig. 1 are directly calculated using Eq. (1), while the simulated values between S_u of any two points are calculated based on 1000 implementations using the MATLAB function corr(su1, su2, "type", "Pearson"). As depicted in Fig. 1, the simulated values of autocorrelation coefficients in all the three directions closely align with the theoretical values. This confirms the effectiveness of the enhanced KL expansion technique in generating the 3D RF.

Example 2. *This case study is based on the research conducted by* Wang et al. (2021), *and* Fig. 2 *illustrates the geometry and grid division of the slope. In total,* 8126 *finite difference grids are divided into different types*: 7746 *hexahedra,* 106 *trihedra,* 182 *pyramids, and* 92 *tetrahedra. These grids are composed of* 9523 *nodes. The boundary conditions for this example are set as follows*: *the bottom* ($Z = 0$ m) *is fully fixed, and the following sides are constrained by vertical rollers*: *the front* ($X = 0$ m), *the rear* ($X = 50$ m), *the left* ($Y = 0$ m), *and the right* ($Y = 50$ m) *following* Wang et al. (2021). Table 2 *presents the values of soil parameters* (*unit weight* γ, *cohesion* c, *internal friction angle* φ, *Poisson's ratio* ν *and Young's modulus* E). *It is worth noting that the values of all soil parameters and boundary conditions are aligned with* Wang et al. (2021).

Firstly, based on the means of soil parameters, the factor of safety (FS), computed using the self-developed finite difference strength

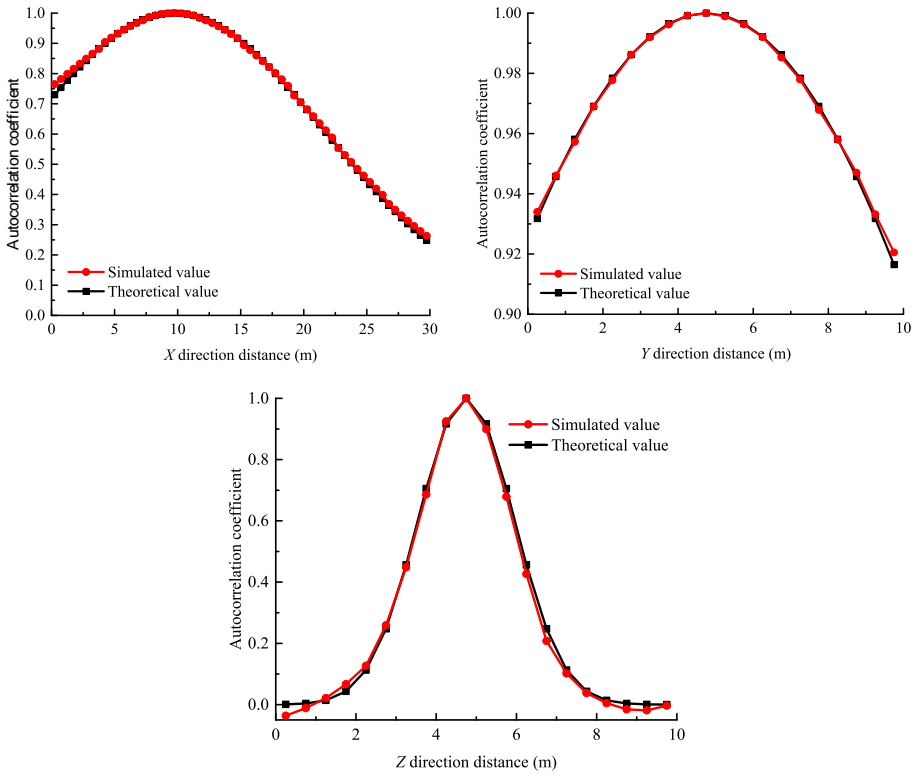

Fig. 1. Comparison of the simulated and theoretical values of autocorrelation coefficients in the three directions of the undrained shear strength random field at the reference point.

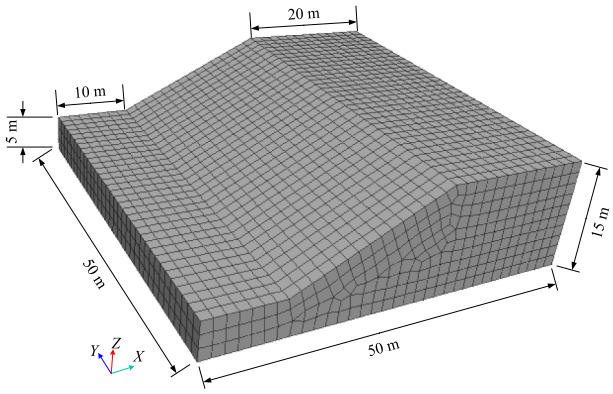

Fig. 2. FDM model of the three-dimensional slope.

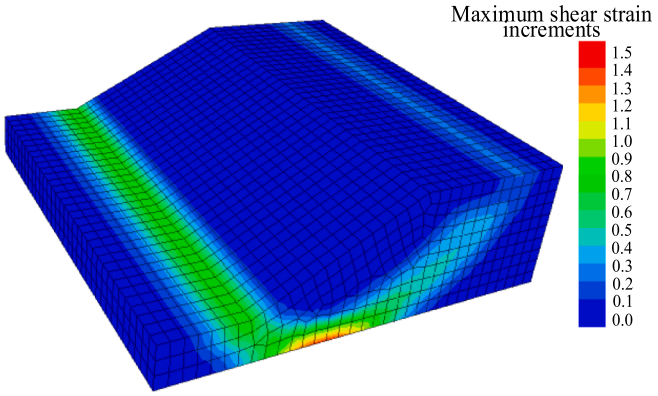

Fig. 3. Deterministic slope stability results ($FS_{min} = 1.08$).

Table 2
Values of soil parameters for the slope.

Parameters	γ (kN/m^3)	c (kPa)	φ (°)	ν	E (MPa)
Mean	20	3	19.6	0.25	10
COV	/	0.28	0.29	/	/

reduction method in FLAC3D (Jiang et al., 2023), is determined as 1.08, which agrees closely with the result of 1.031 obtained by Wang et al. (2021). Fig. 3 presents the corresponding contour plot, illustrating the spatial distribution of maximum shear strain increments. Subsequently, the proposed enhanced KL expansion technique is employed to establish Gaussian RF models for the cohesion and internal friction angle of the slope region. The RF region has a dimension of 50 m × 50 m × 15 m. The cohesion and internal friction angle are assumed to independently follow a normal distribution without cross-correlation. Eq. (1) is also used to simulate the spatial autocorrelation of cohesion and internal friction angle. The autocorrelation distances in the three directions are set as $l_x = 25$ m, $l_y = 25$ m and $l_z = 2$ m, which align with the values used by Wang et al. (2021). To simplify the computational procedure, the coordinates of all RF grid centroids are aligned with those of the finite difference grid centroids. Based on the method used to determine the number of eigenmodes of KL expansion in Example 1, it is established that the number of eigenmodes of 250 is sufficient to meet the accuracy requirements. Thus, discretization of the bivariate RFs requires a total of 500 random variables. The implementations of the bivariate RFs are successively assigned to the corresponding finite difference grids using the element traversal method integrated into FLAC3D. Fig. 4 depicts an implementation of the 3D RFs for the cohesion and internal friction angle of the slope.

Finally, the Latin Hypercube Sampling (LHS) technique (McKay et al., 2000) is used to obtain 1000 sets of 3D RFs implementations of soil parameters. The self-developed finite difference shear reduction

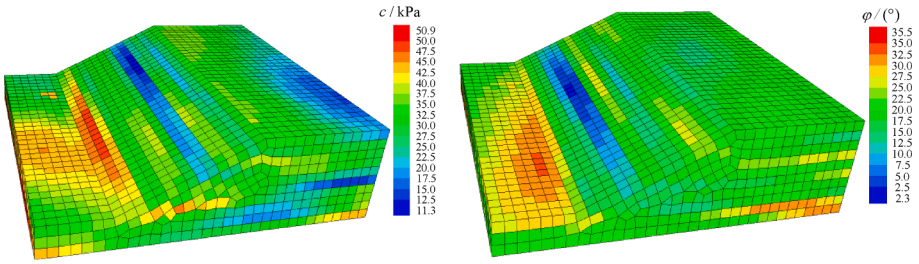

(a) Cohesion (b) Internal friction angle

Fig. 4. One typical random field implementation of soil parameters for the three-dimensional slope.

program is then employed to conduct slope stability analysis on all the RFs implementations, deriving the factors of safety. The calculated probability of failure is 0.43, which is in basic agreement with that 0.43 evaluated by Wang et al. (2021), who utilized the DCT method to simulate the 3D spatial variability of soil parameters. These results further confirm the effectiveness of the proposed enhanced KL expansion technique.

2.3. Evaluation of large deformation characteristics by GIMP

After obtaining the implementations of the 3D RFs of soil parameters, the large deformation characteristic parameters of each implementation can be evaluated by MPM analysis. However, the original MPM has grid-crossing instability, which is caused by the discontinuous gradient of shape functions (Bardenhagen, 2002). A sudden change of the stress can be found when a material point crosses to a new cell. This deficiency can be alleviated by using the generalized interpolation material point method (GIMP) that introduces an alternative grid shape function, S_I, and particle characteristic function, $\chi_p(x)$ (Bardenhagen and Kober, 2004). In the particle domain, the particle characteristic function is generally defined as

$$\chi_p(x) = \begin{cases} 1, x \in \Omega_p \\ 0, otherwise \end{cases} \tag{17}$$

The function $\chi_p(x)$ is used as a basis for representing the particle data by giving a material point property f_p (i.e., particle density ρ_p, stress σ_{ijp} and volume V_p).

To discretize the space occupied by the grid, a computational grid shape function S_I is introduced and required to be a partition of unity $[\sum S_I(x) = 1, \forall x]$, which is expressed as (Ma et al., 2022b)

$$S_{Ip} = \frac{1}{V_p}\int_{\Omega_p \cap \Omega} \chi_p(x) N_I d\Omega \tag{18}$$

$$S_{Ip,j} = \frac{1}{V_p}\int_{\Omega_p \cap \Omega} \chi_p(x) N_{I,j} d\Omega \tag{19}$$

where N_I is the grid nodal shape function; $S_{Ip,j}$ are the gradients of grid shape function, which are the implicit functions of grid node position x_I, particle position x_p and current particle volume Ω_p. As for this step, the discretization is analogous to the FEM. After the GIMP discretization, the total nodal force f_{iI} can be computed as

$$f_{iI} = f_{iI}^{int} + f_{iI}^{ext} \tag{20}$$

$$f_{iI}^{int} = -\sum_p \sigma_{ijp} S_{Ip,j} V_p \tag{21}$$

$$f_{iI}^{ext} = \sum_p m_p S_{Ip} b_{ip} + \int_{\Gamma_t} S_I(x) \overline{t_i} d\Gamma_t \tag{22}$$

where f_{iI}^{int} and f_{iI}^{ext} are the nodal internal force and nodal external force at node I, respectively; m_p is the mass of particle; b_{ip} is the body force; $\overline{t_i}$ is the surface force; Γ_t is the boundary of surface force. Then, by integrating the momentum equations and applying the boundary conditions, the material point positions and velocities can be computed. In this study, the open-source GIMP program named MPM3D, from the Computational Dynamics Laboratory of Tsinghua University (Zhang et al., 2016), is adopted for the analysis.

2.4. Applied soil constitutive model

The strain softening behavior of geomaterials often exhibits a decrease in the shear strength from peak value to residual value as the plastic strain increases (e.g., Liu et al., 2019; Liu et al., 2022). To be more consistent with engineering practice, it is essential to adequately account for the stress–strain relationship of the geomaterials and take the soil softening process into account in the slope failure analysis. In this study, the Drucker-Prager model is utilized to simulate the soil elastoplastic behavior with linear strain softening, incorporating an undrained shear strength as follows (e.g., Bandara and Soga, 2015; Liu et al., 2019):

$$\begin{cases} S_u(\overline{\varepsilon_p}) = S_{u_0} + H\overline{\varepsilon_p}, \overline{\varepsilon_p} < \overline{\varepsilon_{pr}} \\ S_u(\overline{\varepsilon_p}) = S_{ur}, \overline{\varepsilon_p} \geqslant \overline{\varepsilon_{pr}} \end{cases} \tag{23}$$

where S_{u0} and S_{ur} are the initial and residual shear strengths, respectively; $\overline{\varepsilon_p}$ is the plastic shear strain constant; $\overline{\varepsilon_{pr}}$ is the threshold value of plastic shear strain; H is the softening modulus. Detailed description of the constitutive model in the MPM can be found in Zhang et al. (2016).

However, it should be noted that numerical calculations are often influenced by the grid size when using the strain softening model (e.g., Conte et al., 2010; Galavi and Schweiger, 2010). Previous studies have proposed various solutions to address the issue of grid dependence when incorporating the strain softening models (e.g., Yerro et al., 2016; Soga et al., 2016; Troncone et al., 2022a, 2022b). In this study, the proposed approach utilizes two sets of computational MPM grids: rough and refined. However, the use of strain softening models also introduces the issue of grid dependency. Nonetheless, even if the rough grid cannot accurately calculate the runout distance of the landslide, it does not impact the accuracy of the final calculation results. As long as the rough grid model can adequately capture the change of RFs of soil parameters. This is because the refined grid model ultimately determines the accuracy of the calculation results. Hence, it is only necessary to ensure that the refined grid size has a minimal impact on the final calculation results. In the "Illustrative example" section, the refined grid size will be comprehensively investigated to choose the most appropriate grid size.

2.5. Estimation of post-failure characteristic parameters

Once the soil parameters and constitutive model have been determined, the analysis of slope large deformations can be conducted to estimate the post-failure characteristic parameters. Fig. 5 depicts the representative characteristic diagram of an unstable slope after failure.

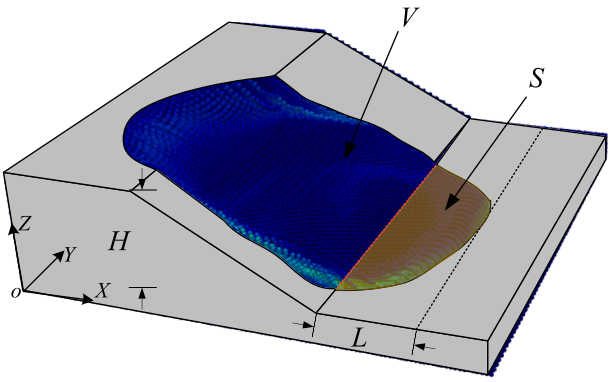

Fig. 5. Typical diagram of the three-dimensional heterogeneous slope after failure.

The failure mode of the slope illustrated in the figure is encapsulated by five key characteristic parameters: relative displacement (R_d), maximum sliding depth (H), maximum runout distance (L), sliding volume (V) and influence area (S). The determination of particle sliding behavior is usually facilitated by assessing R_d, enabling the identification of slope instability. The R_d of a particle can be obtained by, its coordinate positions at the initial moment (x_0, y_0, z_0) and at the final moment (x_t, y_t, z_t), and computed by the Euclidean distance $\sqrt{(x_t - x_0)^2 + (y_t - y_0)^2 + (z_t - z_0)^2}$ between the two coordinates. Conventionally, slope instability is deemed to occur when the maximum value of R_d for all particles exceeds 1.0 m according to the literature (e.g., Liu et al., 2019; Liu et al., 2023). H is an important parameter for identifying the slope failure mode (Liu et al., 2019). S represents the area covered by the landslide body after the slope toe, which can quantify the degree of impact on the infrastructure and residential areas below the slope after slope failure. The definitions of L, H and V are explained in detail in the literature (e.g., Hicks et al., 2014; Chen et al., 2021; Huang et al., 2021), and will not be repeated here.

2.6. Implementation workflow

In order to probabilistically simulate the post-failure behavior of landslides considering the 3D spatial variability of soil parameters, the GIMP is integrated with the RF theory within the LHS framework. To overcome the significant computational challenges using the GIMP, a new CSMPM method is proposed, which involves creating two sets of MPM grid models to enhance collaborative analysis, specifically tailored

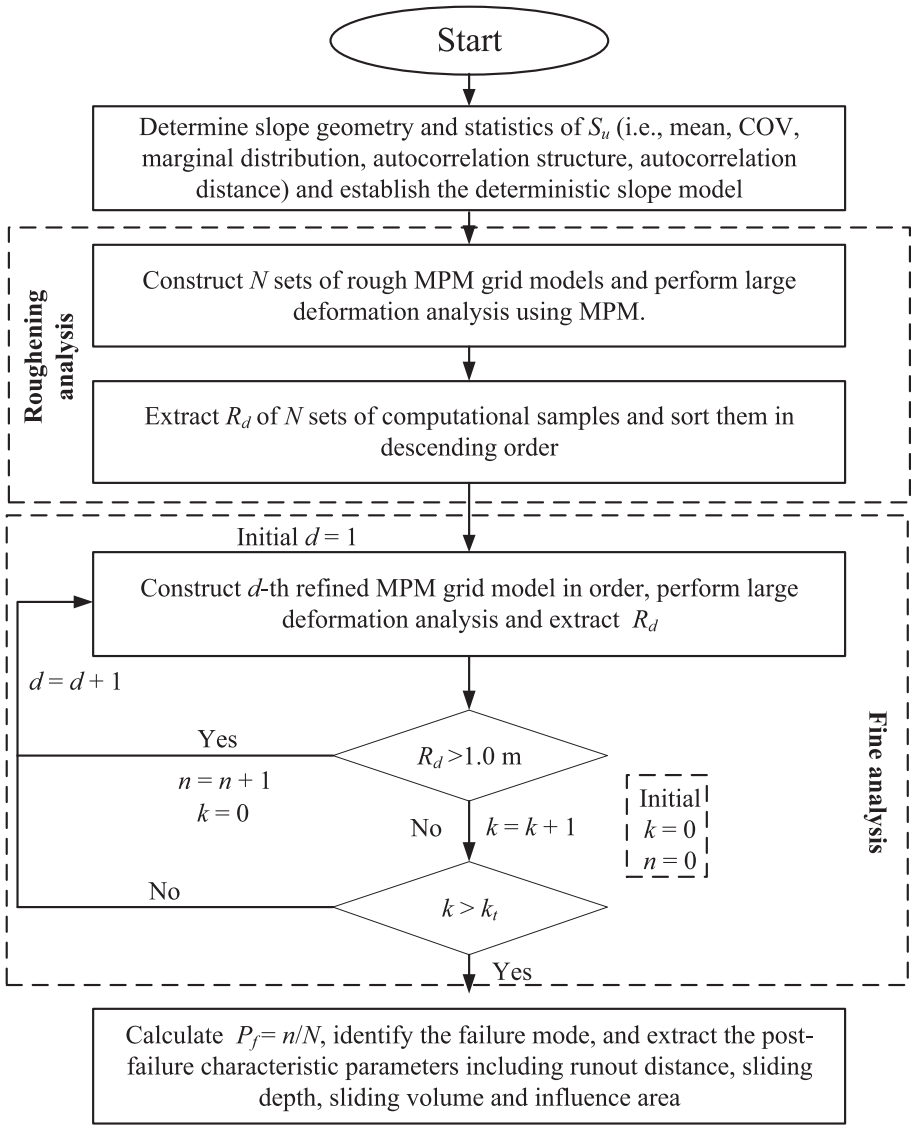

Fig. 6. Flowchart for the implementation of the proposed approach.

for 3D slopes. Initial pre-analysis capitalizes on the computational efficiency of the rough grid model. Subsequently, the samples with elevated hazard levels are identified based on the results from the pre-analyzed samples. Finally, a comprehensive analysis is conducted using the refined grid model, offering a detailed exploration of the probabilistic post-failure behavior of 3D slopes. This method not only optimizes the computational resources but also ensures a nuanced understanding of the landslide risk by prioritizing the examination of the samples with higher hazard potential. Fig. 6 shows the workflow for implementation of the proposed approach. The details are summarized in the following steps:

1. Determine the input information, including slope geometry and statistics of S_u (i.e., mean, COV, marginal distribution, autocorrelation function, autocorrelation distances) and establish the deterministic slope model.
2. Construct N sets of rough MPM grid models using the LHS technique. Perform pre-analysis with each rough grid model. Extract the maximum values of R_d associated with the N sets of computational samples and sort them in descending order.
3. According to the pre-analysis descending order, the refined MPM grid model is constructed for the d-th sample. The initial value of d is 1. Perform in-depth analysis for the d-th sample. Extract the maximum value of R_d for the refined grid model.
4. Judge whether R_d is greater than 1.0 m. If R_d is greater than 1.0 m, go to Step 3. Perform in-depth analysis for the $(d+1)$-th sample. Otherwise, $k = k+1$, the initial $k = 0$. The calculation terminates only when there are k_t consecutive samples with R_d less than 1.0 m. k_t is generally selected as 1–10 % of the total number of samples (Liu et al., 2019). In addition, n is evaluated as the number of samples with large deformation failures.
5. Calculate the probability of slope large deformation failure, $P_f = n/N$, to identify the associated failure modes, and extract the post-failure characteristic parameters including the runout distance, sliding depth, sliding volume and influence area. Estimate the corresponding best-fit probability distributions and statistical characteristics of the post-failure characteristic parameters for various failure modes.

2.7. Illustrative Example

An 3D clay slope example is investigated to show the feasibility of the proposed CSMPM on calculating the probability of slope large deformation failure, identifying the associated failure modes, and evaluating the post-failure characteristic parameters. Fig. 7 shows the geometry of slope with a height of 12 m and a slope angle of 26.6° (1:2). Hicks et al. (2014) found that the results of 3D slope calculations were not affected by the boundary when $L_Y/H > 8$, where L_Y was the length of the Y direction and H was the slope height. To this end, we set L_Y to 96 m since $H = 12$ m. Zhang et al. (2003) found that the computational accuracy was more satisfactory when the distance from the slope toe to the right end boundary was 1.5H and the distance from the slope crest to the left end boundary was 2.5H. In addition, considering the need for large deformation analysis in this study, the runout distance needs to be reserved for the right boundary, so the distance from the slope toe to the right end boundary is taken as 42 m, and the distance from the slope crest to the left end boundary is taken as 30 m. Initially, two MPM grid models are established for the analysis: the rough and refined grid models. The former has a background grid size of 2 m × 2 m × 2 m, with 42,624 material points placed in the Y direction spacing of 1 m and in the X direction spacing of 0.5 m. The latter has a background grid size of 1 m × 1 m × 1 m, with 681,984 material points placed in the X and Y directions spacing of 0.25 m. The RF grid size is consistent with the background grid size. Both models have the same boundary conditions; the X and Y directions of the slope bottom ($Z = 0$ m), the right ($Y = 0$ m), and the left ($Y = 60$ m) sides of the slope are completely fixed, while the front ($X = 60$ m) and rear ($X = 0$ m) sides of the slope are constrained by vertical rollers following Xiao et al. (2016).

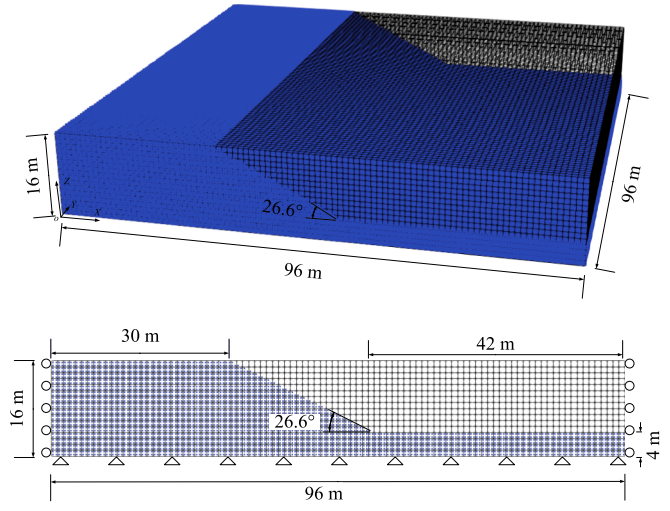

Fig. 7. Three-dimensional slope numerical model and its size.

Assuming that the S_u follows a lognormal distribution with a mean of 42 kPa and a COV of 0.3. The squared exponential autocorrelation function shown in Eq. (1) is also used here to simulate the spatial autocorrelation of undrained shear strength, with $l_x = 60$ m, $l_y = 60$ m and $l_z = 2$ m, respectively. The unit weight, Young's modulus, and Poisson's ratio of the soil are taken as 20 kN/m^3, 100 MPa, and 0.3, respectively. These parameters are treated as deterministic, as their contributions on the slope post-failure characteristic parameters are not remarkable as reported in Cheuk et al. (2013). The residual undrained shear strength is set as 50 % of the original strength. The softening modulus is set as 85 kPa. The initial in situ stresses are generated using gravitational loading. The gravity acceleration is 9.81 m/s^2. The total duration of simulation for the calculation is 20 s, with each time step taking 8.24 × 10^{-4} s wherein the soil deposits become stable according to kinematic energy and unbalanced force of the system (Ma et al., 2022b).

2.8. Deterministic analysis using material point strength reduction method

In this section, the example is modeled deterministically, i.e., as a homogeneous slope, to provide the benchmark for the subsequent probabilistic analysis. First, deterministic analysis is conducted on both MPM grid models with the given values of soil parameters. The undrained shear strength of soil is reduced by a strength reduction factor R, i.e., $S_{u,re} = S_{u,or}/R$. The slope failure occurs when the R increases to a specific value using the material point strength reduction method (Jiang et al., 2022b), which defines the factor of safety. This study adopts the maximum value of R_d as a criterion to determine whether the slope occurs in large deformation failure, using a threshold value of 1.0 m according to Liu et al. (2019) and Liu et al. (2023). Fig. 8(a), (b), (c) and (d), illustrate the final depositions of the slope when the reduction factor is equal to 1.25, 1.26, 1.14 and 1.15, respectively. It is shown that the slope remains stable when $R = 1.25$ and 1.14 but fails when $R = 1.26$ and 1.15, indicating that the factors of safety obtained from the rough and refined grid models are 1.26 and 1.15, respectively. These match with the factor of safety (1.14) obtained from the refined model using the finite difference strength reduction method. On a regular computer equipped with a 12th generation 2.10 GHz Intel(R) Core(TM) i7-12700 desktop, the computation time required for the rough and refined grid models is 407 s and 12,240 s, respectively, indicating that the computation time for the refined grid model is 30.1 times that for the rough grid model.

The above findings highlight that the refined grid model demonstrates the commendable computational accuracy, whereas the rough grid model excels in the computational efficiency. The rough grid model

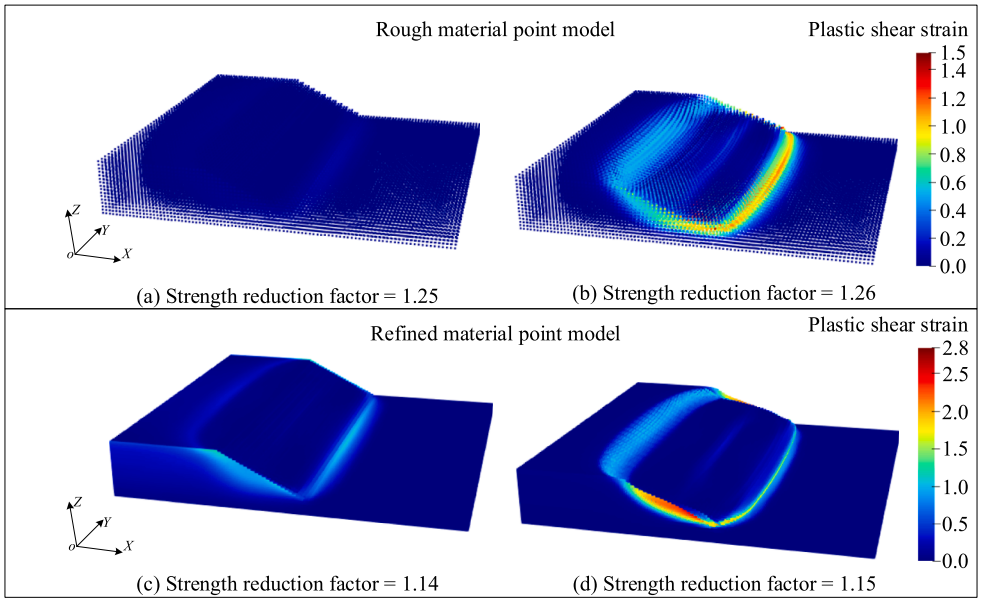

Fig. 8. Comparison of the plastic shear strain contours of slope under different strength reduction factors.

does not significantly impact the accuracy of the final calculation results, even if it fails to precisely calculate the runout distance as long as the rough grid model adequately captures the variation of RF implementation. This is due to the refined grid model being the ultimate determinant of calculation results. In this regard, the refined grid size significantly influences the accuracy of the calculation results. Hence, it is imperative to assess the appropriateness of selecting a 1.0 m grid size for the refined grid model. As such, the MPM grid models with sizes of 0.5 m and 0.75 m are thoroughly compared with the 1.0 m grid model concerning the factor of safety (FOS), runout distance, and calculation time, as shown in Table 3. The calculation results indicate that setting the grid size to less than 1.0 m yields minimal improvement in the calculation accuracy, while exponentially increasing the computation time, thus justifying the selection of a 1.0 m grid size for the refined grid model. Moreover, the errors observed in the computational outcomes for both grid models fall within an acceptable and manageable range. These outcomes serve as the underpinning for the proposed CSMPM, leveraging the complementary strengths of both grid models to establish a robust foundation.

2.9. Probabilistic analysis using CSMPM

In this section, the CSMPM is initially employed to compute the probability of large deformation failure in the 3D slopes. The resulting calculations are juxtaposed with those obtained through the traditional stochastic finite difference method to validate the efficacy and efficiency of the proposed CSMPM. Following this, the CSMPM is utilized to investigate the influence of varying horizontal autocorrelation distances on the probability of 3D slope large deformation failure. Subsequently, an automatic identification of associated failure modes is conducted for all the failure samples based on the sliding depth. The analysis examines into the evolution mechanisms, failure processes and hazards associated with the four identified failure modes in detail. Finally, an examination is undertaken to understand the impact of different horizontal autocorrelation distances on the large deformation failure modes of the 3D slope.

Table 3
Comparison of calculation results of various refined grid sizes.

Grid size (m)	FOS	Runout distance (m)	Computation Time (s)
1	1.15	14.17	12,240
0.75	1.15	14.52	24,503
0.5	1.15	14.76	48,976

2.10. Calculation of probability of large deformation failure

The CSMPM accomplishes the discretization of 3D RF of S_u through the enhanced KL expansion technique. The use of the KL expansion method for RF discretization is notable due to its independence from the MPM background grid size. This independence is pivotal in ensuring the seamless execution of the cooperative analysis process. Fig. 9 depicts the RF implementations of undrained shear strength generated using both the rough and refined grid models. Observing Fig. 9 reveals that while the rough grid model does not achieve the same level of continuity as the refined grid model, it still captures the overall distribution characteristics of the RF of undrained shear strength.

To ensure sufficient failure samples for subsequent large deformation failure analysis in slopes, $N = 1000$ sets of RF implementations are generated using the LHS as input. The pre-analysis is carried out based

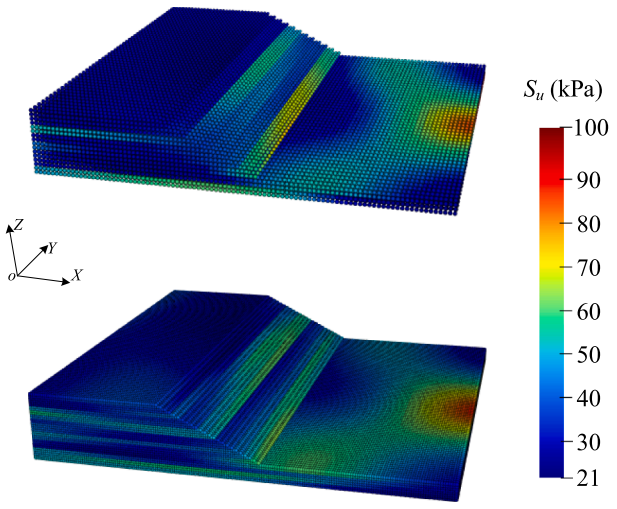

Fig. 9. Comparison of the random field implementations based on rough and refined grid models.

on the rough grid model, and the maximum value of R_d for each sample are extracted. At the same time, the failure samples in the pre-analysis are sorted from large to small according to R_d, and the refined grid model is used to carry out in-depth analysis in turn, and to judge whether the slope large deformation failure occurs. A total of 280 sets of samples needs to be deeply analyzed, from which 244 sets of large deformation failure samples are obtained. The final calculated probability of slope failure is 0.244, which is basically consistent with that (0.231) calculated by the finite difference strength reduction method in FLAC3D under the same parameter condition. It should be noted that the proposed CSMPM can be implemented using a parallel computing strategy (i.e., simultaneous calculation of ten iterations, achieving 100 % CPU utilization on a regular computer). The computation time required for 1000 rough grid model evaluations is 11.3 h, while 280 refined material point grid model evaluations require 92.4 h, resulting in a total of 106.5 h. It can be found that the computational efficiency is significantly higher than that of the traditional SMPM, especially for the slope reliability evaluation with low failure probabilities ($<10^{-3}$), where the advantages of the proposed approach in terms of the computational efficiency are much more evident.

2.11. Effect of horizontal autocorrelation distance on probability of slope failure

Further investigations are conducted using the proposed approach to demonstrate the influence of the autocorrelation distance in the horizontal direction (X and Y directions) on the probability of slope large deformation failure. The autocorrelation distance in the horizontal direction ranges from 10 to 120 m, while the autocorrelation distance in the vertical direction (Z direction) is set at 2 m. Furthermore, when one autocorrelation distance in the horizontal direction is changed, the other autocorrelation distance in the horizontal direction remains unchanged at 60 m. Fig. 10 depicts the relationship curve between the probability of slope failure and the horizontal autocorrelation distance. In Fig. 10, the probability of slope failure increases with increasing the horizontal autocorrelation distance. It can be observed that when the horizontal autocorrelation distance is less than 60 m, it has a significant impact on the probability of slope failure. In addition, the horizontal autocorrelation distances in the X and Y directions are essentially close to each other in terms of their effect on the probability of slope failure. However, does this necessarily mean that the horizontal autocorrelation distances in the X and Y directions have the same effect on the post-failure behavior of landslides? A comprehensive analysis of the effect of horizontal autocorrelation distance on the large deformation failure modes of the 3D slope is necessarily conducted.

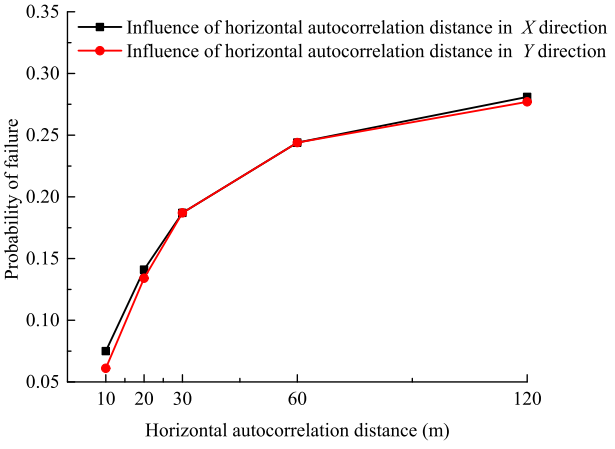

Fig. 10. Variation of the probability of slope failure changing with the horizontal autocorrelation distance.

2.12. Large deformation failure modes analysis

For each failure sample, the large deformation failure mode of the slope can be automatically identified through the analysis of a refined grid model using the proposed approach. Based on the maximum sliding depth, the slope failure modes can be categorized into shallow and deep failure modes. Additionally, there are compound failure mode involving spatial and temporal factors, as well as progressive failure mode. The slope failure modes are classified as follows: (1) Shallow failure mode, which occurs at the slope toe and above, with a sliding depth equal to or less than 12 m. (2) Deep failure mode, which occurs below the slope toe, with a sliding depth greater than 12 m. (3) Compound failure mode, in which both shallow and deep failure modes occur simultaneously at different spatial positions during landslide occurrence. (4) Progressive failure mode, where the slope experiences various failure modes at different time intervals. Fig. 11 shows the evolution process of a typical shallow failure mode of the slope and the associated cross-section at $Y = 70$ m. Initially, a sliding mass forms above the slope toe, which continues sliding along the foundation. The shallow failure mode of the slope exhibits a fan-shaped spreading phenomenon along the Y direction, which is consistent with engineering practice and cannot be captured by a 2D analysis. Fig. 12 shows the spatial distribution of undrained shear strength corresponding to this shallow failure mode. As seen from Fig. 12, there is a weak interlayer above the slope toe and the undrained shear strength of the upper soil layer is lower. This is an important factor that triggers the overall shallow failure of the slope.

Fig. 13 shows the evolution process of a typical deep failure mode of the slope and the associated cross-section at $Y = 48$ m. From Fig. 13, it can be observed that a depth of damage is deeper than the slope base. The sliding volume is significantly larger than that corresponding to the shallow failure mode, which leads to more severe consequences. Fig. 14 presents the spatial distribution of undrained shear strength corresponding to this deep failure mode. As seen from Fig. 14, there is a weak interlayer or zone present in both the upper and lower layers of the slope, resulting in an overall deep failure mode that permeates through the slope vertically.

In addition, Fig. 15 shows the evolution process of a typical compound failure mode of the slope and the associated cross-sections at $Y = 10$ m and $Y = 80$ m. From Fig. 15, it can be observed that the left-side region of the slope is dominated by shallow failure mode, while the right-side region is dominated by deep failure mode. Although the compound failure mode incorporates the characteristics of both shallow and deep failure modes, it also possesses unique characteristics. The presence of deep failure inhibits the development and spreading of shallow failure, resulting in varying runout distances in the X direction. This feature highlights the necessity to consider the spatial variability of geotechnical parameters in the study of large deformation failure modes of slopes. Even though the sliding volume corresponding to this failure mode falls between those of shallow and deep failure modes, the uncertainty in the runout distance along the X direction poses difficulties for landslide disaster prevention and control. Fig. 16 demonstrates the spatial distribution of undrained shear strength corresponding to this compound failure mode. As seen from Fig. 16, the cause of shallow failure on the left-side region is primarily influenced by the weak interlayer, while the cause of deep failure on the right-side region is the presence of weak zones both above and below, leading to the occurrence of through failure in the slope.

Fig. 17 presents the evolution process of a typical progressive failure mode of the slope and the associated cross-section at $Y = 48$ m. Comparing Fig. 17 with Fig. 13, it can be observed that although the initial failure process of the progressive failure mode is similar to that of the deep failure mode. After 10 s of the first failure occurrence in the slope, a new secondary shallow failure happens due to the presence of a weak interlayer at the rear edge of the slope. In addition, compared to the deep failure mode, the progressive failure mode involves multiple releases of gravitational potential energy, resulting in more severe

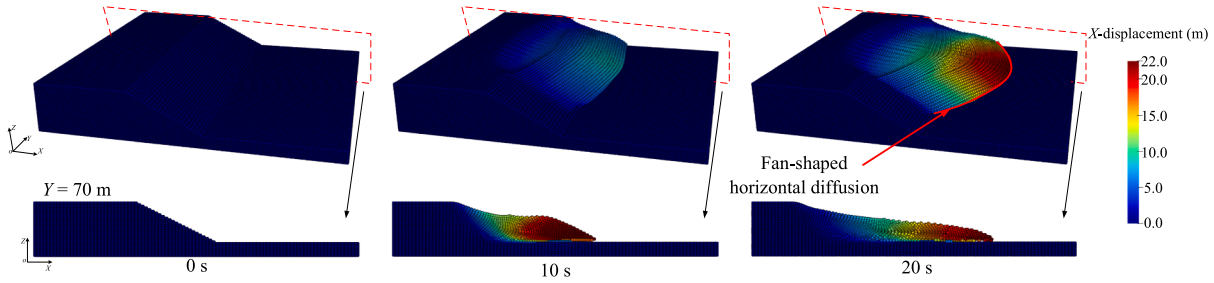

Fig. 11. Evolution processes of a typical shallow failure mode of the slope and its cross-section of $Y = 70$ m.

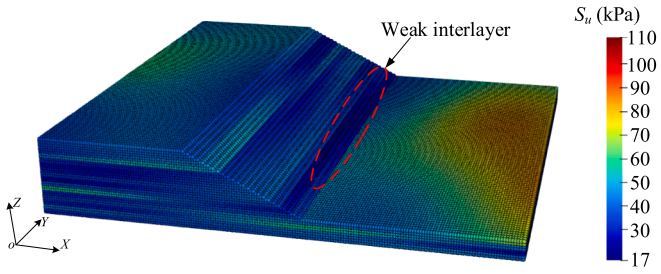

Fig. 12. Spatial distribution of the undrained shear strength corresponding to a typical shallow failure mode of slope.

consequences. Fig. 18 displays the spatial distribution of undrained shear strength corresponding to the progressive failure mode. Like the deep failure mode, the presence of weak zones in the upper and lower layers leads to the through failure in the slope. After the initial failure occurs, the upper soil layer at the rear edge of the slope undergoes the secondary shallow failure due to the loss of support.

Based on the above, it can be concluded that the different spatial distributions of soil parameters lead to different slope failure modes and their evolution processes, resulting in varying consequences. To further estimate the deformation characteristic parameters underlying different failure modes, the Akaike information criterion (*AIC*) (Akaike, 1974) and Bayesian information criterion (*BIC*) (Schwarz, 1978) are used as evaluation indices to determine the best-fit probability distributions of the influence area, sliding volume and runout distance corresponding to different failure modes (e.g., Zhang et al., 2018; Ma et al., 2022a).

$$AIC = -2\sum_{i=1}^{N}\ln[f(q_i)] + 2k_1 \tag{17}$$

$$BIC = -2\sum_{i=1}^{N}\ln[f(q_i)] + k_1 \ln N \tag{18}$$

where q_i is the characteristic parameter calculated by the proposed CSMPM, including influence area (S), sliding volume (V), or runout distance (L), $i = 1, 2, \ldots, N$, in which N is the sample size; $f(q_i)$ represents the selected probability density function; k_1 is the number of model parameters for the selected probability density function. Taking the influence area as an example, Table 4 compares the best-fit probability distributions of the influence area for different failure modes based on the principle of minimum values of *AIC* and *BIC*. Table 5 further lists the best-fit probability distributions for the post-failure characteristic parameters underlying different failure modes. Fig. 19 compares the best-fit probability distributions of three characteristic parameters for different failure modes. As seen from Fig. 19, the ranking of the severity levels of different failure modes can readily deduced as follows: progressive > deep > compound > shallow. Clearly, the progressive failure mode may cause the most severe consequences and requires giving special attention. The uncertainty of the runout distance of shallow failure mode is greater due to the wide range of parameter distribution. In contrast, the distributions of runout distance for the progressive, deep and compound failure modes are relatively concentrated and close to each other.

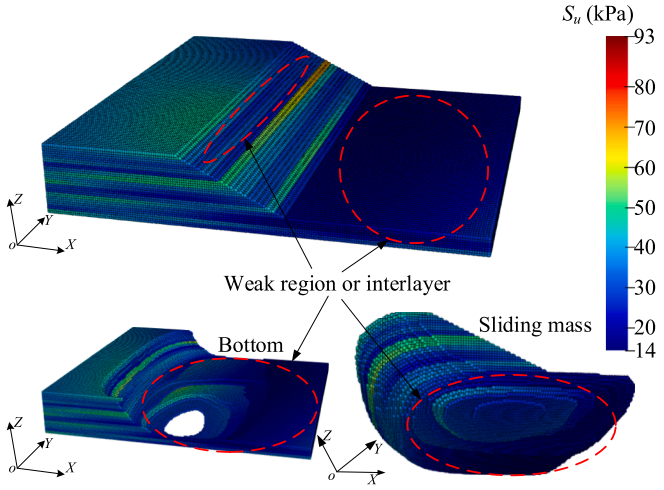

Fig. 14. Spatial distribution of the undrained shear strength corresponding to a typical deep failure mode of slope.

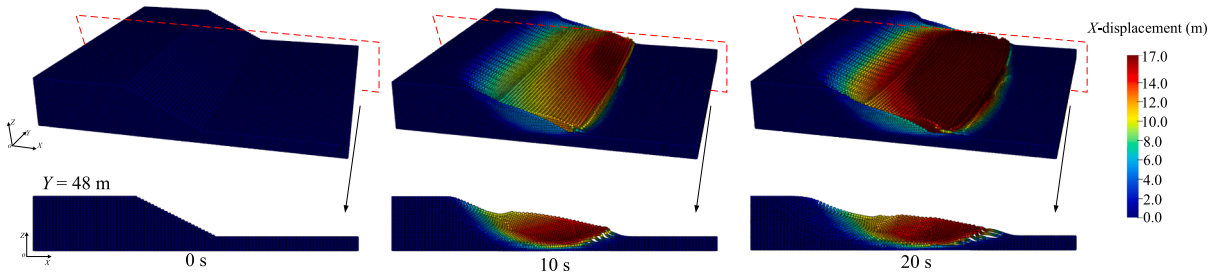

Fig. 13. Evolution processes of a typical deep failure mode of the slope and its cross-section of $Y = 48$ m.

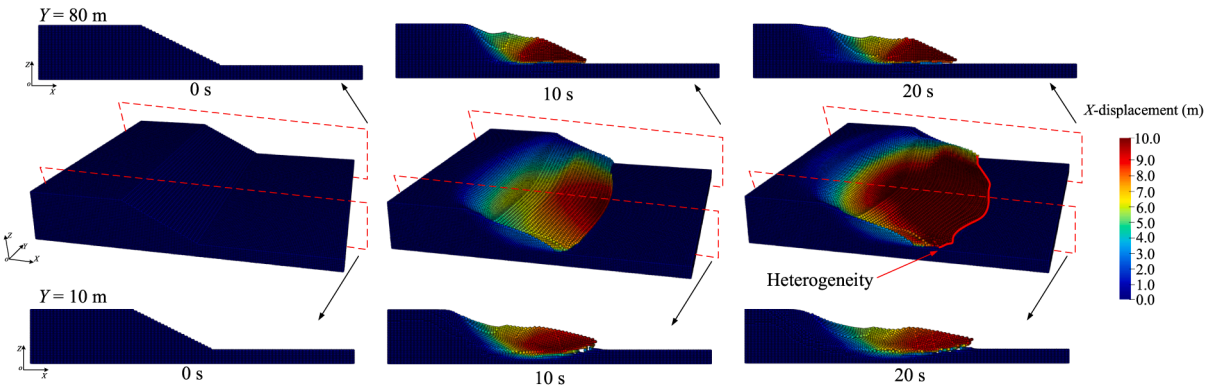

Fig. 15. Evolution processes of a typical compound failure mode of the slope and its cross-sections of $Y = 10$ m and $Y = 80$ m.

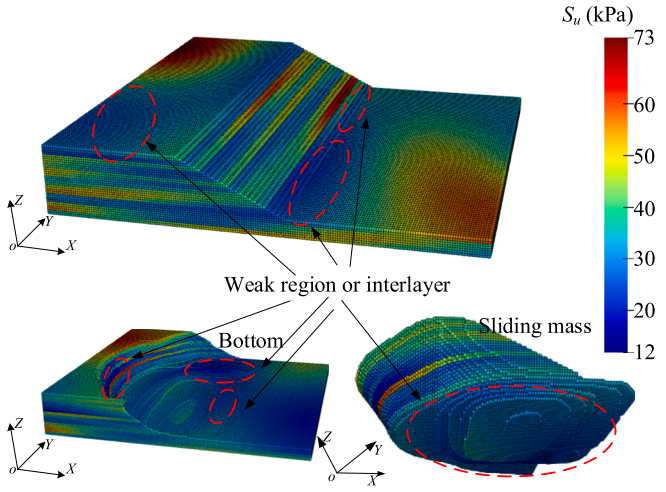

Fig. 16. Spatial distribution of undrained shear strength corresponding to a typical compound failure mode of slope.

2.13. Effect of horizontal autocorrelation distance on slope failure modes

Finally, to illustrate the influence of the horizontal (X and Y directions) autocorrelation distance on the large deformation failure modes of the slope, Fig. 20(a) and (b) compare the variation curves of the ratios of different failure modes with respect to the autocorrelation distances in the X and Y directions, respectively. The dominant failure mode of the slope is the deep failure mode, which exhibits considerably higher ratio compared to the other failure modes. Based on the data from Fig. 20(a), the ratio of deep failure mode decreases as the autocorrelation distance in the X direction increases, while the ratios of shallow and progressive failure modes initially increase and then subsequently decrease. The ratio of compound failure mode exhibits a trend of initial increase, followed by a decrease, and subsequently a slight rise as the autocorrelation distance in the X direction increases. Fig. 20(b) reveals that the ratio of shallow failure mode increases as the autocorrelation distance in the Y direction increases. The ratio of deep failure mode initially decreases and then slightly increases with the increase of the autocorrelation distance in the Y direction, while the trend in the ratio of progressive failure mode is the opposite. The ratio of compound failure mode decreases with increasing the autocorrelation distance in the Y direction and eventually reaches a stable state.

3. Discussion

This paper introduces a novel approach, termed CSMPM, aimed at addressing the challenges related to the probabilistic characterization of slope large deformations considering the 3D spatial variability of soil parameters. This holistic methodology can play a crucial role in enhancing our understanding of the post-failure behaviors in 3D slopes, offering a valuable tool for accurate risk assessments in geotechnical engineering. The proposed approach is utilized to identify four prevalent large deformation failure modes in practical engineering scenarios. The subsequent analysis of these failure mechanisms provides new perspectives that could guide future strategies for mitigating landslide

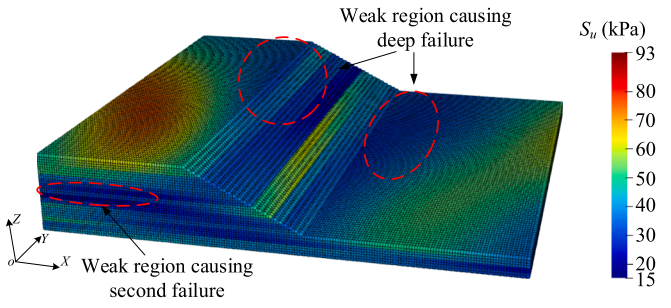

Fig. 18. Spatial distribution of undrained shear strength corresponding to a typical progressive failure mode of slope.

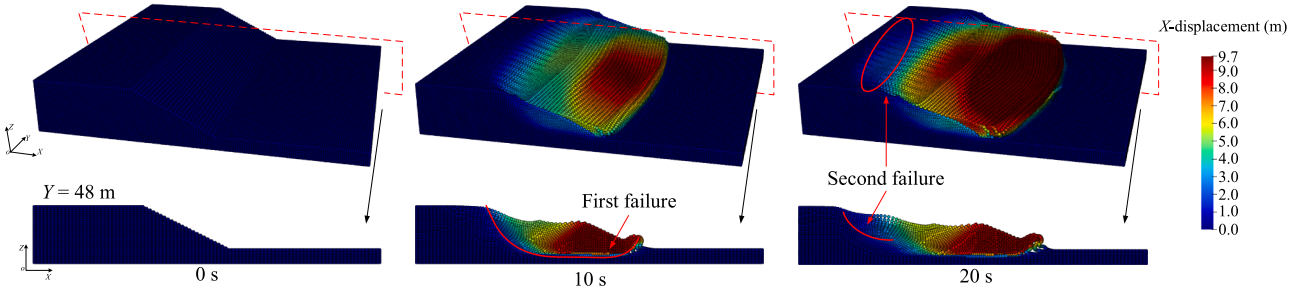

Fig. 17. Evolution processes of a typical progressive failure mode of the slope and its cross-section of $Y = 48$ m.

Table 4
Best-fit probability distributions of the influence area corresponding to different slope failure modes.

Failure mode	Evaluation index	Normal	Logistic	Gamma	Weibull	Optimum
Shallow failure	*AIC*	**205.87**	206.15	207.90	206.15	Normal
	BIC	**207.15**	207.43	209.18	207.43	
Deep failure	*AIC*	**15192.1**	15239.8	15195.6	15208.6	Normal
	BIC	**15202.0**	15249.6	15205.5	15218.5	
Compound failure	*AIC*	**2549.04**	2553.52	2576.47	2553.29	Normal
	BIC	**2555.39**	2559.88	2582.82	2559.64	
Progressive failure	*AIC*	5064.75	**5064.70**	5081.07	5076.15	Logistic
	BIC	5072.48	**5072.44**	5088.80	5083.88	

Table 5
Best-fit probability distributions of characteristic parameters corresponding to different slope failure modes.

Failure mode	Influence area (*S*)	Slide volume (*V*)	Runout distance (*L*)
Shallow failure	Normal	Logistic	Normal
Deep failure	Normal	Logistic	Normal
Compound failure	Normal	Logistic	Normal
Progressive failure	Logistic	Weibull	Normal

disasters.

The runout process of the landslide presents a challenging dynamic large deformation scenario, characterized by significant strains that induce partial soil remodeling and softening. Particularly in highly sensitive soils, the soil strength experiences a substantial decline attributed to the strain softening phenomenon. However, the simplified linear softening Mohr-Coulomb failure criterion employed in this study may fail to accurately capture the strength reduction of the soil under escalating strains. Consequently, the employment of advanced constitutive models that can account for the intricate strain-softening behavior of soil becomes imperative in the slope large deformation analysis to achieve a more realistic simulation of soil deformation.

This study focused only on the soils in horizontally deposited horizons. However, inclined stratified slopes are frequently observed in nature (Ma et al., 2022b). The geometric relationship between a slope and underlying layers/strata may considerably influence the post-failure behavior. Extensive research has been conducted to investigate the influence of anisotropic sedimentary stratigraphy on the destabilization mechanism or runout distance of 2D slopes (e.g., Zhu et al., 2019; Wang et al., 2021; Huang and Leung, 2021; Ng et al., 2022; Ma et al., 2022b). Further research is necessary to explore the effects of the rotational anisotropy in common soil parameters on the large deformation failure modes in 3D slopes. This is attributed to the more complex and realistic layering direction and failure modes of 3D slopes compared to 2D scenarios.

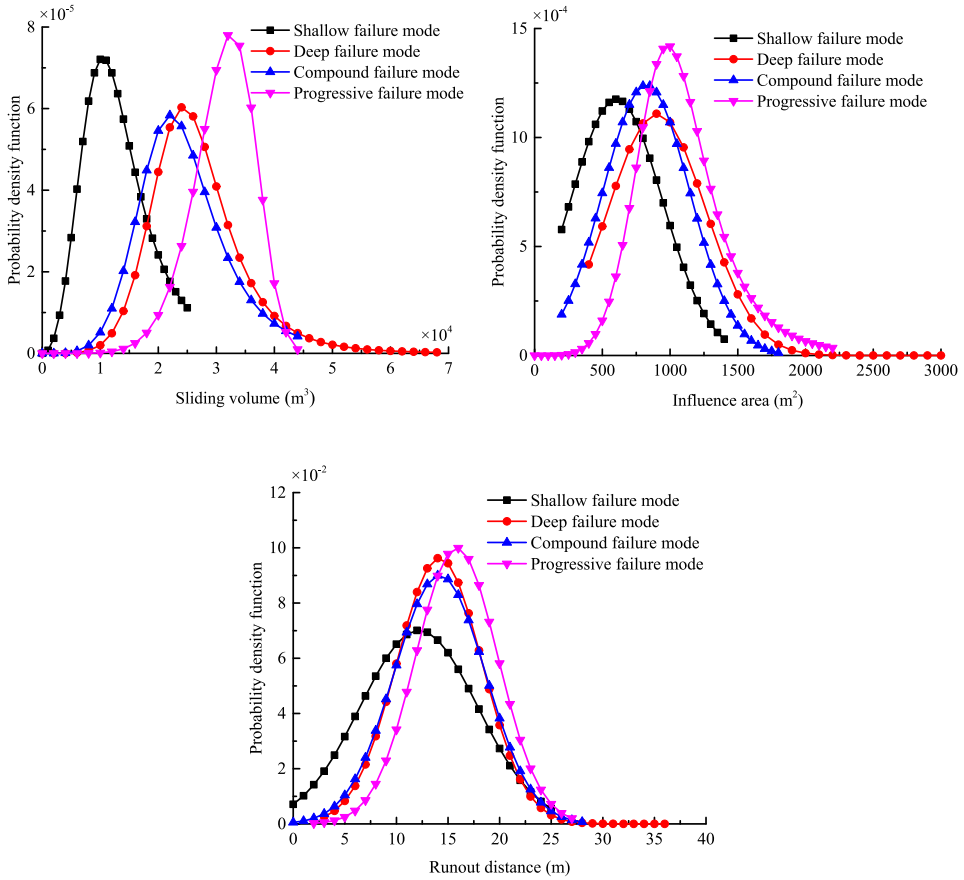

Fig. 19. Comparison of the best-fit probability distributions of three post-failure characteristic parameters corresponding to different slope failure modes.

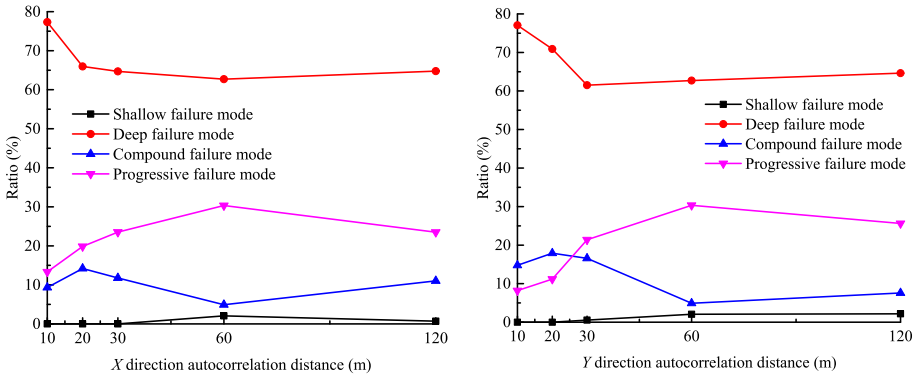

(a) Influence of X direction autocorrelation distance

(b) Influence of Y direction autocorrelation distance

Fig. 20. Influence of the horizontal autocorrelation distances on the ratios of different slope failure modes.

4. Conclusions

This paper proposes a novel CSMPM that integrates the 3D spatial variability of soil parameters for conducting probabilistic analysis of large deformation failures in slopes. The primary goal of this approach is to accurately calculate the large deformation failure probabilities of 3D heterogeneous slopes, identify the associated various failure modes, and assess the post-failure characteristics. The key conclusions of this study can be summarized as follows:

(1) The study develops an enhanced KL expansion method that effectively simulates the 3D spatial variability of geotechnical parameters. Through matrix decomposition, this method overcomes limitations associated with inadequate computer memory in handling the huge 3D autocorrelation coefficient matrix, thereby enhancing the computational efficiency. Notably, it is not constrained by grid coordinates, thus laying the groundwork for subsequent probabilistic analysis of large deformation failures in slopes.

(2) The proposed CSMPM involves developing two distinct sets of background grid models to enable collaborative analysis. The approach is superior to the traditional SMPM in terms of the computational efficiency and thus provides an effective tool for the probabilistic analysis of large deformation failures of 3D heterogeneous slopes.

(3) The study explores the influence of horizontal autocorrelation distance on the large deformation failure probability of the slope using the proposed CSMPM. The results show that the probability of failure increases with the increase of horizontal autocorrelation distance. The horizontal autocorrelation distance below 60 m significantly impacts the probability of failure. The effects of horizontal autocorrelation distances in the X and Y directions on the probability of failure are basically close to each other.

(4) The proposed CSMPM automatically identifies multiple diverse failure modes, including shallow, deep, compound and progressive. The shallow failure mode occurs due to the presence of weak interlayer above the slope toe, which exhibits fan-shaped diffusion, while the shallow failure mode occurs due to upper and lower weak regions being penetrated. The compound failure mode has strong heterogeneity of the runout distance along the Y direction. The progressive failure mode with multiple gravity releases has the highest hazard. Additionally, it prioritizes their severity degrees as progressive > deep > compound > shallow.

(5) The analysis of the 3D soil spatial variability highlights the deep failure as the dominant mode. Specifically, as the autocorrelation distance in the X direction increases, the ratio of deep failure mode decreases, while the ratios of shallow and progressive failure modes show an initial decrease followed by an increase. The compound failure mode exhibits a pattern of initial increase, subsequent decrease, and slight rise. In contrast, in the Y direction, the ratio of deep failure mode initially decreases and then slightly increases, whereas the ratio of progressive failure mode demonstrates the opposite trend. The ratio of compound failure mode decreases with increasing the autocorrelation distance in the Y direction until reaching a stable state. These findings highlight the complex effect of the autocorrelation distances in two horizontal directions on the slope large deformation failure modes.

CRediT authorship contribution statement

Shui-Hua Jiang: Writing – review & editing, Validation, Supervision, Resources, Methodology, Funding acquisition, Conceptualization. **Jian-Ping Li:** Writing – original draft, Visualization, Software, Project administration, Methodology, Investigation, Formal analysis, Conceptualization. **Guo-Tao Ma:** Writing – review & editing, Validation, Supervision, Methodology, Conceptualization. **Mohammad Rezania:** Writing – review & editing, Validation.

Declaration of competing interest

The authors declare that they have no known competing financial interests or personal relationships that could have appeared to influence the work reported in this paper.

Data availability

Data will be made available on request.

Acknowledgments

This work was supported by the National Natural Science Foundation of China (Grant Nos. 52222905, 52179103, 42272326), Research Fund for International Scientists (Grant Nos. 52150610492 and 52350610265) and Jiangxi Provincial Natural Science Foundation (Grant Nos. 20224ACB204019 and 20232ACB204031). The financial supports are gratefully acknowledged.

References

Akaike, H., 1974. A new look at the statistical model identification problem. Ieee. T. Automat. Contr. Control. 19, 716.

Bandara, S., Ferrari, A., Laloui, L., 2016. Modelling landslides in unsaturated slopes subjected to rainfall infiltration using material point method. Int. J. Numer. Anal. Met. 40 (9), 1358–1380.
Bandara, S., Soga, K., 2015. Coupling of soil deformation and pore fluid flow using material point method. Comput. Geotech. 63, 199–214.
Bardenhagen, S.G., 2002. Energy conservation error in the material point method for solid mechanics. J. Comput. Phys. 180 (1), 383–403.
Bardenhagen, S.G., Kober, E.M., 2004. The generalized interpolation material point method. C. Comput. Model. Eng. Sci. 5, 477–495.
Chen, X., Li, D., Tang, X., Liu, Y., 2021. A three-dimensional large-deformation random finite-element study of landslide runout considering spatially varying soil. Landslides 18 (9), 3149–3162.
Chen, K.T., Wu, J.H., 2018. Simulating the failure process of the Xinmo landslide using discontinuous deformation analysis. Eng. Geol. 239, 269–281.
Chen, L.L., Zhang, W.G., Chen, F.Y., Gu, D.M., Wang, L., Wang, Z.Y., 2022. Probabilistic assessment of slope failure considering anisotropic spatial variability of soil properties. Geosci. Front. 13 (3), 101371.
Cheuk, C.Y., Ho, K.K.S., Lam, A.Y.T., 2013. Influence of soil nail orientations on stabilizing mechanisms of loose fill slopes. Can. Geotech. J. 50 (12), 1236–1249.
Cho, S.E., 2010. Probabilistic assessment of slope stability that considers the spatial variability of soil properties. J. Geotech. Geoenviron. 136 (7), 975–984.
Chowdhury, R.N., Xu, D.W., 1995. Geotechnical system reliability of slopes. Reliab. Eng. Syst. Safe. 47 (3), 141–151.
Conte, E., Silvestri, F., Troncone, A., 2010. Stability analysis of slopes in soils with strain-softening behaviour. Comput. Geotech. 37 (5), 710–722.
Conte, E., Pugliese, L., Troncone, A., 2020. Post-failure analysis of the Maierato landslide using the material point method. Eng. Geol. 277, 105788.
Coombs, W.M., Augarde, C.E., Brennan, A.J., Brown, M.J., Charlton, T.J., Knappett, J.A., Motlagh, Y.G., Wang, L., 2020. On Lagrangian mechanics and the implicit material point method for large deformation elasto-plasticity. Comput. Methods Appl. Mech. Eng. 358, 112622.
Deng, Z.P., Li, D.Q., Qi, X.H., Cao, Z.J., Phoon, K.K., 2017. Reliability evaluation of slope considering geological uncertainty and inherent variability of soil parameters. Comput. Geotech. 92, 121–131.
Galavi, V., Schweiger, H.F., 2010. Nonlocal multilaminate model for strain softening analysis. Int. J. Geomech. 10 (1), 30–44.
Hicks, M.A., Nuttall, J.D., Chen, J., 2014. Influence of heterogeneity on 3D slope reliability and failure consequence. Comput. Geotech. 61, 198–208.
Hu, L., Takahashi, A., Kasama, K., 2022. Effect of spatial variability on stability and failure mechanisms of 3D slope using random limit equilibrium method. Soils. Found. 62 (6), 101225.
Huang, L., Leung, Y.F., 2021. Reliability assessment of slopes with three-dimensional rotated transverse anisotropy in soil properties. Can. Geotech. J. 58 (9), 1365–1378.
Huang, J., Lyamin, A.V., Griffiths, D.V., Krabbenhoft, K., Sloan, S.W., 2013. Quantitative risk assessment of landslide by limit analysis and random fields. Comput. Geotech. 53, 60–67.
Jiang, S.H., Li, D.Q., Zhang, L.M., Zhou, C.B., 2014. Slope reliability analysis considering spatially variable shear strength parameters using a non-intrusive stochastic finite element method. Eng. Geol. 168, 120–128.
Jiang, S.H., Huang, J., Griffiths, D.V., Deng, Z.P., 2022a. Advances in reliability and risk analyses of slopes in spatially variable soils: a state-of-the-art review. Comput. Geotech. 141, 104498.
Jiang, X., Zhang, P., Lu, Y., Liu, L., Zhang, M., 2022b. Slope failure criterion for the strength reduction material point method. Bull. Geol. Sci. Technol. 41 (2), 113–122 (in Chinese).
Jiang, S.H., Zhu, G.Y., Wang, Z.Z., Huang, Z.T., Huang, J., 2023. Data augmentation for CNN-based probabilistic slope stability analysis in spatially variable soils. Comput. Geotech. 160, 105501.
Lee, S., Ching, J., 2020. Simplified risk assessment for a spatially variable undrained long slope. Comput. Geotech. 117, 103228.
Li, Y.J., Hicks, M.A., Nuttall, J.D., 2015. Comparative analyses of slope reliability in 3D. Eng. Geol. 196, 12–23.
Li, D.Q., Xiao, T., Zhang, L.M., Cao, Z.J., 2019. Stepwise covariance matrix decomposition for efficient simulation of multivariate large-scale three-dimensional random fields. Appl. Math. Model. 68, 169–181.
Liu, L.L., Liang, C.Q., Huang, L., Wang, B., 2023. Parametric analysis for the large deformation characteristics of unstable slopes with linearly increasing soil strength by the random material point method. Comput. Geotech. 162, 105661.
Liu, X., Wang, Y., Li, D.Q., 2019. Investigation of slope failure mode evolution during large deformation in spatially variable soils by random limit equilibrium and material point methods. Comput. Geotech. 111, 301–312.
Liu, Y., Zhang, W., Zhang, L., Zhu, Z., Hu, J., Wei, H., 2018. Probabilistic stability analyses of undrained slopes by 3D random fields and finite element methods. Geosci. Front. 9 (6), 1657–1664.
Liu, Y., Chen, X., Hu, M., 2022. Three-dimensional large deformation modeling of landslides in spatially variable and strain-softening soils subjected to seismic loads. Can. Geotech. J. 60 (4), 426–437.
Ma, G., Rezania, M., Nezhad, M.M., 2022a. Effects of spatial autocorrelation structure for friction angle on the runout distance in heterogeneous sand collapse. Transp. Geotech. 33, 100705.
Ma, G., Rezania, M., Nezhad, M.M., Hu, X., 2022b. Uncertainty quantification of landslide runout motion considering soil interdependent anisotropy and fabric orientation. Landslides 19 (5), 1231–1247.
Ma, G., Rezania, M., Nezhad, M.M., 2022c. Stochastic assessment of landslide influence zone by material point method and generalized geotechnical random field theory. Int. J. Geomech. 22 (4), 04022002.
McKay, M.D., Beckman, R.J., Conover, W.J., 2000. A comparison of three methods for selecting values of input variables in the analysis of output from a computer code. Technometrics 42 (1), 55–61.
Mohammadi, S., Taiebat, H.A., 2013. A large deformation analysis for the assessment of failure induced deformations of slopes in strain softening materials. Comput Geotech 49, 279–288.
Ng, C.W.W., Qu, C., Ni, J., Guo, H., 2022. Three-dimensional reliability analysis of unsaturated soil slope considering permeability rotated anisotropy random fields. Comput. Geotech. 151, 104944.
Phoon, K.K., Huang, S.P., Quek, S.T., 2002. Implementation of Karhunen-Loeve expansion for simulation using a wavelet-Galerkin scheme. Probab. Eng. Mech. 17 (3), 293–303.
Phoon, K.K., Retief, J.V., Ching, J., Dithinde, M., Schweckendiek, T., Wang, Y., 2016. Some observations on iso2394:2015 annex d (reliability of geotechnical structures). Struct. Saf. 62, 24–33.
Schwarz, G., 1978. Estimating the dimension of a model. Ann. Stat. 461–464.
Shu, S., Ge, B., Wu, Y., Zhang, F., 2023. Probabilistic assessment on 3D stability and failure mechanism of undrained slopes based on the kinematic approach of limit analysis. Int. J. Geomech. 23 (1), 06022037.
Soga, K., Alonso, E., Yerro, A., Kumar, K., Bandara, S., 2016. Trends in large-deformation analysis of landslide mass movements with particular emphasis on the material point method. Géotechnique. 66 (3), 248–273.
Troncone, A., Pugliese, L., Conte, E., 2022a. Analysis of an excavation-induced landslide in stiff clay using the material point method. Eng. Geol. 296, 106479.
Troncone, A., Pugliese, L., Parise, A., Conte, E., 2022b. A simple method to reduce mesh dependency in modelling landslides involving brittle soils. Geotech. Lett. 12 (3), 167–173.
Troncone, A., Pugliese, L., Parise, A., Conte, E., 2023. A practical approach for predicting landslide retrogression and run-out distances in sensitive clays. Eng. Geol. 326, 107313.
Varkey, D., Hicks, M.A., Vardon, P.J., 2023. Effect of uncertainties in geometry, inter-layer boundary and shear strength properties on the probabilistic stability of a 3D embankment slope. Georisk 17 (2), 262–276.
Wang, B., Hicks, M.A., Vardon, P.J., 2016. Slope failure analysis using the random material point method. Geotech. Lett. 6 (2), 113–118.
Wang, Z., Wang, H., Xu, W., 2021. Effect of rotated anisotropy of soil shear strength on three-dimensional slope stability: a probabilistic analysis. B. Eng. Geol. Environ. 80 (8), 6527–6538.
Weng, M.C., Lin, M.L., Lo, C.M., Lin, H.H., Lin, C.H., Lu, J.H., Tsai, S.J., 2019. Evaluating failure mechanisms of dip slope using a multiscale investigation and discrete element modelling. Eng. Geol. 263, 105303.
Xiao, T., Li, D.Q., Cao, Z.J., Au, S.K., Phoon, K.K., 2016. Three-dimensional slope reliability and risk assessment using auxiliary random finite element method. Comput. Geotech. 79, 146–158.
Yerro, A., Alonso, E.E., Pinyol, N.M., 2016. Run-out of landslides in brittle soils. Comput. Geotech. 80, 427–439.
Yerro, A., Girardi, V., Martinelli, M., Ceccato, F., 2022. Modelling unsaturated soils with the material point method. a discussion of the state-of-the-art. Geomech. Energy Environ. 32, 100343.
Zhang, X., Chen, Z., Liu, Y., 2016. The material point method: a continuum-based particle method for extreme loading cases. Academic Press.
Zhang, W., Ji, J., Gao, Y., 2020. SPH-based analysis of the post-failure flow behavior for soft and hard interbedded earth slope. Eng. Geol. 267, 105446.
Zhang, L., Li, J., Li, X., Zhang, J., Zhu, H., 2018. Rainfall-induced soil slope failure: stability analysis and probabilistic assessment. CRC Press.
Zhang, L., Gong, W.P., Li, X.X., Tan, X.H., Zhao, C., Wang, L., 2022. A comparison study between 2D and 3D slope stability analyses considering spatial soil variability. J. Zhejiang. Univ-Sc. A. 23 (3), 208–224.
Zhang, L.Y., Zhen, Y.R., Zhao, S.Y., Shi, W.M., 2003. The feasibility study of strength-reduction method with FEM for calculating safety factors of soil slope stability. J. Hydraul. Eng. 1, 21–27 (in Chinese).
Zhu, B., Hiraishi, T., 2023. A decomposed Karhunen-Loève expansion scheme for the discretization of multidimensional random fields in geotechnical variability analysis. Stoch. Environ. Res. Risk Assess. 38, 1215–1233.
Zhu, B., Hiraishi, T., Mase, H., Baba, Y., Pei, H., Yang, Q., 2021. A 3-D numerical study of the random wave-induced response in a spatially heterogenous seabed. Comput. Geotech. 135, 104159.
Zhu, H., Zhang, L.M., Xiao, T., 2019. Evaluating stability of anisotropically deposited soil slopes. Can. Geotech. J. 56 (5), 753–760.